Kelvin-Helmholtz Instability Simulation

ASTRON 255 FINAL PROJECT

University of California, Berkeley

Ruoyi Yin

May 9, 2020

Abstract

Kelvin Helmholtz Instability (KHI) is a crucial concept in fluid dynamics and it exists in many astrophysical events. Therefore, analyzing the consistency and understanding the distinctions between numerical and analytical solutions are crucial for evaluating performance of KHI simulation. We run KHI simulation on Enzo for 3 different resolutions: 128×128, 256×256 and 512×512 grid points, and compare results with analytical growth rate and a reference numerical growth rate derived from Pencil Code to better assess Enzo performance. The results demonstrate that there is a relatively large difference between analytical and Enzo result that could be explained by both physical and numerical reasons. After all, Enzo simulation is in relatively good agreement with Pencil Code reference solution, and more detailed analyses would provide insights and guidance for future research work.

1 Introduction

Kelvin-Helmholtz Instability (KHI) is initially studied qualitatively by Helmholtz and quantitatively by Kelvin. This instability arises when two parts of fluids have different horizontal velocity, and most of the time also different density, leading to a discontinuity at the interface. If perturbations exist on the interface, the velocity orthogonal to the interface would grow and the flow would eventually develop into vortices. KHI are used to describe shear flows with negligible viscosity. In astrophysics, KHI is involved in research work related to stellar interiors, protoplanetary disk, galaxy medium, etc [2, 7, 11].

Open source hydrodynamical simulation codes have been frequently used by people to aid their analyses or model the behavior of astrophysical systems. In this report, we use Enzo, a Eulerian adaptive mesh refinement grid-based code, to conduct numerical simulations for KHI [3]. The performance of Enzo is evaluated by comparing two values, maximum y-direction specific kinetic energy and y-velocity mode amplitude, with an analytical solution and Pencil Code reference solution [10].

The classical growth rate is derived in Chandrasekhar [4] for KHI with sharp discontinuity on the interface and incompressible flow over an infinite region. However, Enzo simulation is run for a smooth transition interface and compressible flow over a finite region. Therefore, the numerical solutions derived from Enzo would be different from the classical growth rate. Besides, we also compare Enzo solutions with a reference numerical solution from Pencil Code, a high order finite difference code [10].

In section 2, we would introduce the methods we use to derive Enzo, analytical and reference result. In section 3, we present the simulation results, the comparison between solutions for maximum y-direction specific kinetic energy and y-velocity mode amplitude, and the Enzo result for a longer time period when KHI develops into non-linear regime. In section 4, we detailedly discuss both physical and numerical reasons for differences among analytical, Enzo and reference results, and provide explanations for a secondary instability in non-linear regime. In section 5, we conclude our work and provide insights for future analyses.

2 Method

2.1 Enzo Simulation

2.1.1 Enzo Parameters

We run 2-dimensional Enzo simulations with 3 different grid resolutions: 128×128, 256×256 and 512×512. This problem uses periodic boundary conditions for compressible flow and smooth transition layer.

The equations are solved by using piecewise parabolic method (PPM), with a nonlinear Riemann solver. Courant safety number is chosen to be 0.4.

For initial conditions, the inner density is 2, outer density is 1; the inner velocity is -0.5, outer velocity is 0.5; the pressure is 2.5; the bulk velocity is 0; the perturbation amplitude is 0.01; the ramp smoothing parameter is 0.025 [10, 13]. The smooth transition in density across interfaces is defined as:

$$
\begin{aligned}
\rho = \rho_1 - \rho_m e^{(y-0.25)/L} & \quad if \ -1/4 > y > -1/2 \\
\rho = \rho_2 + \rho_m e^{-(y-0.25)/L} & \quad if \ 0 > y \geq -1/4 \\
\rho = \rho_2 + \rho_m e^{-(0.75-y)/L} & \quad if \ 1/4 > y \geq 0 \\
\rho = \rho_1 - \rho_m e^{-(y-0.75)/L} & \quad if \ 1/2 > y \geq 1/4
\end{aligned}
\tag{1}
$$

where

$$
\rho_m = (\rho_1 - \rho_2)/2
\tag{2}
$$

The smooth transition in velocity across interfaces is defined as:

$$
\begin{aligned}
V = V_1 - V_m e^{(y-0.25)/L} & \quad if \ -1/4 > y > -1/2 \\
V = V_2 + V_m e^{-(y-0.25)/L} & \quad if \ 0 > y \geq -1/4 \\
V = V_2 + V_m e^{-(0.75-y)/L} & \quad if \ 1/4 > y \geq 0 \\
V = V_1 - V_m e^{-(y-0.75)/L} & \quad if \ 1/2 > y \geq 1/4
\end{aligned}
\tag{3}
$$

where

$$
V_m = (V_1 - V_2)/2
\tag{4}
$$

The simulation results are displayed later for two time intervals: $t \in (0, 1.5)$ for linear growth rate comparisons and $t \in (0, 4)$ for discussion about non-linear growth and instability. The time-step is $\Delta t = 0.02$. A sinusoidal perturbation for y-velocity is defined as:

$$
V_y = 0.01 sin(4\pi x)
\tag{5}
$$

2.1.2 Post-Simulation Calculations

We use two metrics for different-solution comparison: maximum y-direction specific kinetic energy and y-velocity mode amplitude. The former value represents an extremum, which would give us insights about Enzo's performance for noise reduction, since this value is sensitive to noise in y-velocity calculation. The latter value is an average y-velocity value over all simulation grids, displaying the general trends of y-velocity evolution with time.

The former value is calculated directly by choosing the maximum $1/2\rho V_y^2$ over all of the grids. The latter value is more complicated to derive and involves Fourier Transform. The equations used to derive the latter value are [10]:

$$
\begin{aligned}
s_i &= V_y sin(4\pi x) \ e^{-4\pi|y+0.25|} \quad if \ y < 0 \\
s_i &= V_y sin(4\pi x) \ e^{-4\pi|y-0.25|} \quad if \ y \geq 0
\end{aligned}
\tag{6}
$$

$$
\begin{aligned}
c_i &= V_y cos(4\pi x) \ e^{-4\pi|y+0.25|} \quad if \ y < 0 \\
c_i &= V_y cos(4\pi x) \ e^{-4\pi|y-0.25|} \quad if \ y \geq 0
\end{aligned}
\tag{7}
$$

$$
\begin{aligned}
d_i &= e^{-4\pi|y+0.25|} \quad if \ y < 0 \\
d_i &= e^{-4\pi|y-0.25|} \quad if \ y \geq 0
\end{aligned}
\tag{8}
$$

$$
M = 2\sqrt{\left(\frac{\Sigma_{i=1}^{N} s_i}{\Sigma_{i=1}^{N} d_i}\right)^2 + \left(\frac{\Sigma_{i=1}^{N} c_i}{\Sigma_{i=1}^{N} d_i}\right)^2}
\tag{9}
$$

where M is the y-velocity amplitude for each time-step, representing the average performance of Enzo simulation over all grids.

2.1.3 The yt Project & Python Analysis

The extraction of data from simulation and the post-simulation analyses are conducted in Jupyter Notebook [8] by the aid of The yt Project [16], and several Python packages: Numpy [12], Matplotlib [6], SciPy [17] and Astropy [1].

2.2 Analytical Solution

The KHI analytical solution is derived for incompressible flow with sharp discontinuity over an infinite region [4, 9, 14] .

The initial setup denotes the existence of horizontal velocity and density discontinuities on the interface.

ρ_1, v_1, P_1 represent conditions above the interface, and ρ_2, v_2, P_2 represent conditions below the interface. Initially $\rho_1 \neq \rho_2$, $v_1 \neq v_2$, $P_1 = P_2$, x is the direction that is parallel to the interface, y is orthogonal to the interface.

We first introduce a perturbation to both pressure and velocity:

$$V = V_0 + V'$$
$$P = P_0 + P' \tag{10}$$

$$V_0 = (V_1, 0, 0) \quad z > 0$$
$$V_0 = (V_2, 0, 0) \quad z < 0 \tag{11}$$

The continuity equation is:

$$\frac{\partial \rho}{\partial t} + \nabla \cdot (\rho V) = 0$$
$$\frac{d\rho}{dt} + \rho \nabla \cdot V = 0 \tag{12}$$

Due to incompressibility of the flow, $d\rho/dt = 0$, plugging equation 10 into continuity equation, we get:

$$\nabla \cdot V' = 0 \tag{13}$$

Then, we plug expressions of pressure and velocity with perturbation terms into momentum equation, to the first order:

$$V \cdot \nabla V = (V_0 + V') \cdot \nabla V' = V_0 \cdot \nabla V'$$
$$\rho \left[\frac{\partial}{\partial t} V' + V_0 \cdot \nabla V' \right] = \rho \left[\frac{\partial}{\partial t} V' + V_0 \frac{\partial}{\partial x} V' \right] = -\nabla P' \tag{14}$$

Take the divergence of this equation:

$$\rho \left[\frac{\partial}{\partial t} (\nabla \cdot V') + V_0 \frac{\partial}{\partial x} (\nabla \cdot V') \right] = -\nabla^2 P' \tag{15}$$

From equation 13 and 15, we get:

$$\nabla^2 V' = 0 \tag{16}$$

$$\nabla^2 P' = 0 \tag{17}$$

Therefore, for both pressure and velocity perturbations, we take a specific ansatz to describe their general solutions:

$$f(x,t) = f(y) e^{i(kx - \omega t)} \tag{18}$$

where f(y) would have the form:

$$f(y) = A_1 e^{ky} + A_2 e^{-ky} \tag{19}$$

in order to satisfy the Laplace's equations for pressure and velocity perturbations (equation 16-17). A_1 and A_2 are coefficients determined by initial conditions. Since we require that the pressure calculated from both sides should have the same value, $A_1 = A_2 = A$.

From now on, V and P with subscript 0 denote initial conditions on two sides of the interface. V and P with superscript 0 denote perturbation terms that depend on y, which we would derive through calculations.

For perturbation in pressure, we apply the ansatz (requiring finite pressure at infinity):

$$\begin{aligned} P' &= Ae^{ky}e^{i(kx-\omega t)} \quad if \ y < 0 \\ P' &= Ae^{-ky}e^{i(kx-\omega t)} \quad if \ y > 0 \end{aligned} \tag{20}$$

For perturbation in velocity, since it also satisfies Laplace's equation, we can take the same ansatz:

$$V' = V^0(y)e^{i(kx-\omega t)} \tag{21}$$

where $V^0(y)$ is the value we want to derive. Then, we take the derivative of velocity with respect to t and x separately:

$$\frac{\partial}{\partial x}V' = V^0(y) \times (ik)e^{i(kx-\omega t)} \tag{22}$$

$$\frac{\partial}{\partial t}V' = V^0(y) \times (-i\omega)e^{i(kx-\omega t)} \tag{23}$$

Substituting equation 22 and 23 into momentum equation 14:

$$\rho_0[V^0(y)(kV_0 - \omega)] \times e^{i(kx-\omega t)} = -\frac{\partial}{\partial x}P' = \pm Ae^{\mp ky}e^{i(kx-\omega t)} \tag{24}$$

which gives us:

$$V^0(y) = \pm\frac{kAe^{\mp ky}}{\rho_0(kV_0 - \omega)} \tag{25}$$

Here in equation 25, we equate the imaginary component on both sides of the momentum equation.

Then we consider the perturbation in displacement r:

$$r = r_0 + r' \tag{26}$$

$$\frac{d}{dt}r' = \frac{\partial}{\partial t}r' + V_{0,x}\frac{\partial}{\partial x}r' = V' \tag{27}$$

The general solution for r' also has the form:

$$r' = r^0 e^{i(kx-\omega t)} \tag{28}$$

Plugging equation 21, 28 into equation 27, we get:

$$ir^0(kV_0 - \omega) \times e^{i(kx-\omega t)} = \pm \frac{ikAe^{\mp ky}}{\rho_0(kV_0 - \omega)} \times e^{i(kx-\omega t)} \tag{29}$$

which gives us:

$$r^0 = \pm \frac{kAe^{\mp ky}}{\rho_0(kV_0 - \omega)^2} \tag{30}$$

The displacement in y direction would be:

$$y' = \pm \frac{kAe^{\mp ky}}{\rho_0(kV_0 - \omega)^2} \times sin(kx - \omega t) \tag{31}$$

On the interface (y = 0), therefore, the equation for displacement in y direction calculated from both sides of the interface should be the same:

$$\rho_1(kV_1 - \omega)^2 = -\rho_2(kV_2 - \omega)^2 \tag{32}$$

Expanding the quadratic terms and grouping terms involving $(\omega/k)^2$ and (ω/k):

$$(\rho_1 + \rho_2)\left(\frac{\omega}{k}\right)^2 - 2\left(\frac{\omega}{k}\right)[\rho_1 V_1 + \rho_2 + V_2] + [\rho_1 V_1^2 + \rho_2 + V_2^2] = 0 \tag{33}$$

Solving equation 33, we get:

$$\frac{\omega}{k} = \frac{(\rho_1 V_1 + \rho_2 + V_2) \pm i(V_1 - V_2)(\rho_1\rho_2)^{1/2}}{\rho_1 + \rho_2} \tag{34}$$

$$\frac{\omega_r}{k} = \frac{(\rho_1 V_1 + \rho_2 + V_2)}{\rho_1 + \rho_2]} \qquad \frac{\omega_i}{k} = \frac{\pm(V_1 - V_2)(\rho_1\rho_2)^{1/2}}{\rho_1 + \rho_2} \tag{35}$$

Since in the general perturbation equation, there is an imaginary unit i in front of ω, therefore, after plugging the value of ω back into the general perturbation equation, the ω_r term would only influence phase, the ω_i term would involve real growth of y-direction velocity.

Therefore, the classical growth rate r is (we take the positive value since the negative value represents decaying rate):

$$r = \omega_i = \frac{k|V_1 - V_2|(\rho_1\rho_2)^{1/2}}{\rho_1 + \rho_2} \tag{36}$$

Therefore, plugging in the initial conditions specifically for our simulation, we get $r = 5.924$.

7

2.3 Pencil Code Reference Numerical Solution

Since analytical solutions would be different from Enzo results, we extract Pencil Code numerical solutions as a reference to better assess Enzo simulation performance.

Pencil Code is a high-order finite-difference code for compressible hydrodynamic flows [10].

The maximum y-direction specific kinetic energy and y-velocity mode amplitude are calculated from Pencil Code with 4096×4096 grid points in order to get high resolution that is sufficient for acting as a reference. Other initial conditions are the same as in our Enzo Simulation.

3 Result

3.1 Density Plot

Figure 1 is the density plot for Enzo simulation when $t = 1.5$. The perturbation evolves from the interface and eventually the flow develops into vortices.
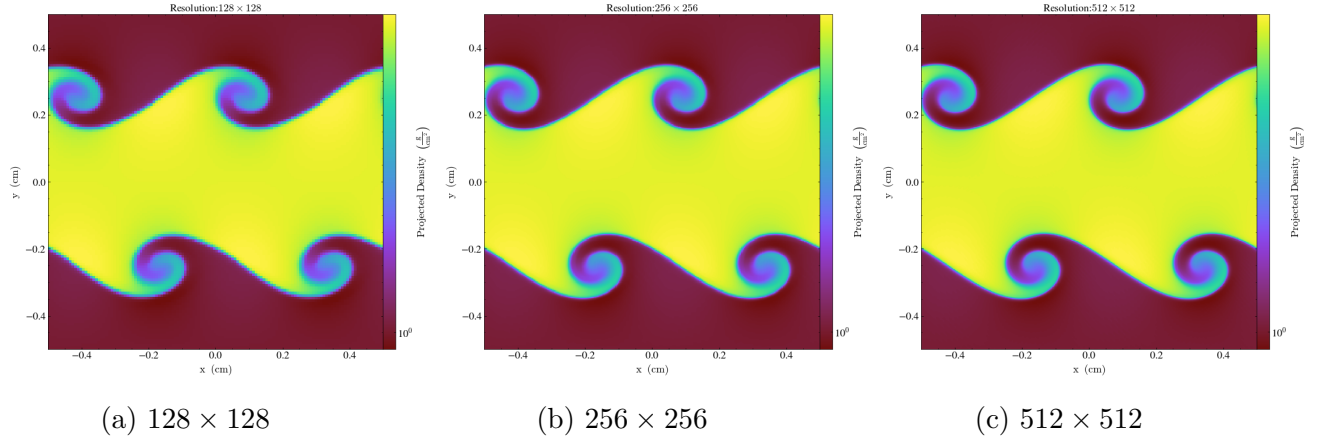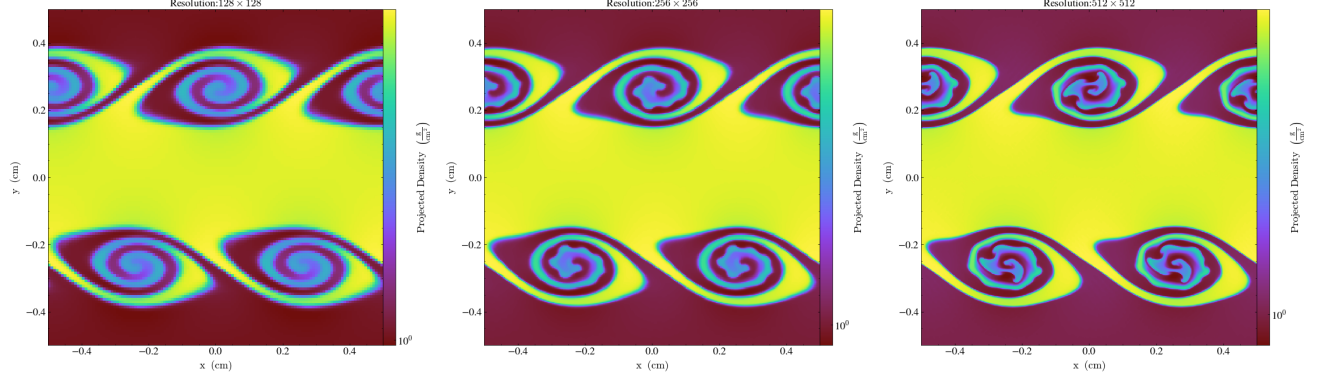

(a) 128×128 (b) 256×256 (c) 512×512

Figure 1: Density plots over all grids for 3 different resolutions when $t = 1.5$.

Figure 2 is the density plot for Enzo simulation when $t = 2.5$. We can see that inside each of the primary instability billow (except for 128×128 grids), there are also small perturbations of specific wave lengths. This wave length cannot be derived quantitatively in our result since it is different for different resolutions. People refer to this instability as the secondary instability in non-linear regime of KHI simulation.

(a) 128×128 (b) 256×256 (c) 512×512

Figure 2: Density plots over all grids for 3 different resolutions when $t = 2.5$.

3.2 Metrics for Comparisons

We introduce two metrics used for comparisons between analytical, Enzo, and reference numerical solutions.

3.2.1 Maximum Y-Direction Specific Kinetic Energy

First, we calculate maximum y-direction specific kinetic energy for Enzo simulation and compare it with Pencil Code reference solution (Figure 3). The analytical solution is not shown in this plot because the growth rate we derived would be better compared in the next metric. This metric is used for identifying Enzo performance regarding extreme values.
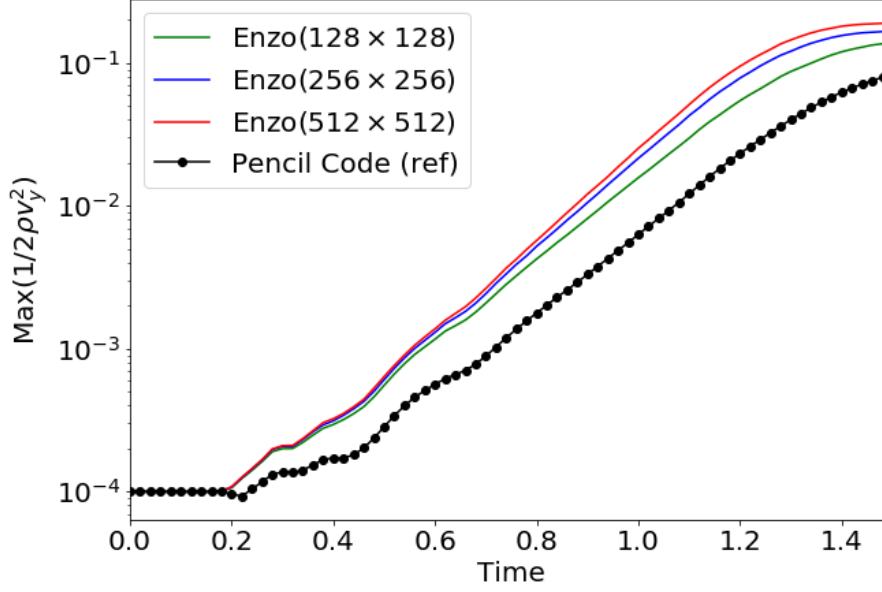
Figure 3: The maximum y-direction specific kinetic energy versus time. The green, blue and red lines denote Enzo result with different resolutions. The black dotted line shows reference result.

Figure 3 shows that when simulations just start for a short period, all numerical simulations return similar results, which possibly comes from the effect of noise. After $t = 0.2$, both simulations show small perturbations or oscillations in their growth, but eventually follow exponential growth with almost constant rates. As simulation grows with time, the difference between Enzo and reference simulations becomes larger, but the slope are still similar. And as the result approaches t = 1.5, the growth rate for both simulations become smaller, denoting the end of linear growth rate regime. One of the explanations for oscillations in their growth is noise developed on the interface in simulations. Eventually as y-direction velocities become larger, their effects are larger than the effects from noise and the curves then follow relatively constant exponential growth.

The Enzo simulation with different resolutions return results close to each other. With higher resolution, the maximum y-direction specific kinetic energy value is relatively larger.

This plot shows that Enzo simulation performs well and the noise developed in simulation would not significantly affect the overall result.

3.2.2 Y-Velocity Mode Amplitude

Then, we focus on the average performance of Enzo simulation. By applying the Fourier Transform method in section 2.1.2, we calculate y-velocity amplitude specifically for $k = 4\pi$ mode at each time-step and compare it with both analytical and Pencil Code Reference solutions (Figure 4).
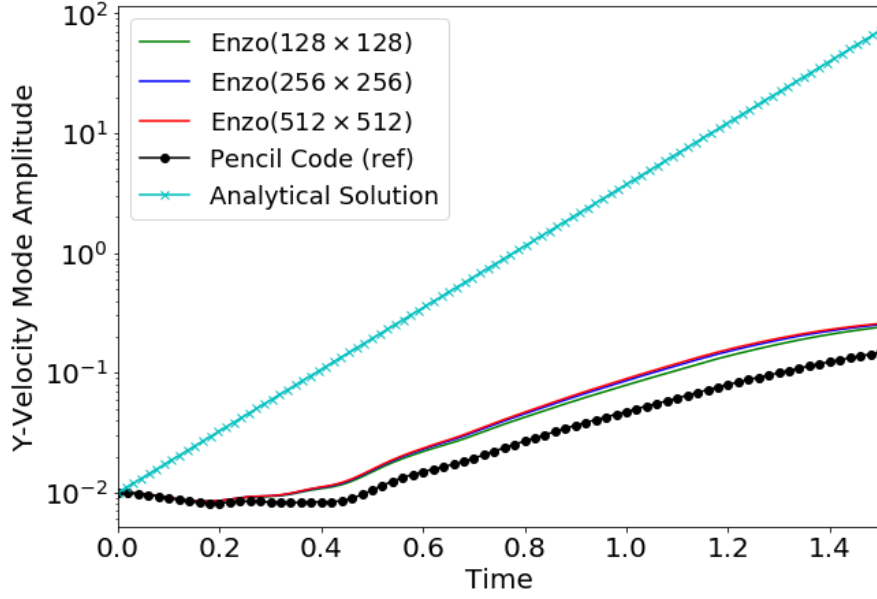
10

Figure 4: The average y-velocity mode amplitude over all grids versus time. The green, blue and red lines denote Enzo result with different resolutions. The black dotted line shows reference result. The cyan color line represents analytical growth rate solution ($r = 5.924$).

Figure 4 demonstrates the comparison between analytical, Enzo, and reference solutions. Analytical solution applies the growth rate calculated in section 2.2. It is clear that the analytical growth rate is larger than the other two. The reasons for this distinction will be detailedly explained in section 4.

Focusing on the comparison between Enzo and Pencil Code simulations, we find that at first there are some oscillations, but later as the simulation develops, both values show exponential growth trend with relatively constant growth rate.

The difference between Enzo result of distinct resolutions are not clear in this plot as they squeeze in one place. They would be further discussed later in section 4.

3.3   Non-linear Regime

After the linear exponential growth rate regime, the flow enters the non-linear regime. We run simulations for all 3 resolutions until $t = 4$ (Figure 5).
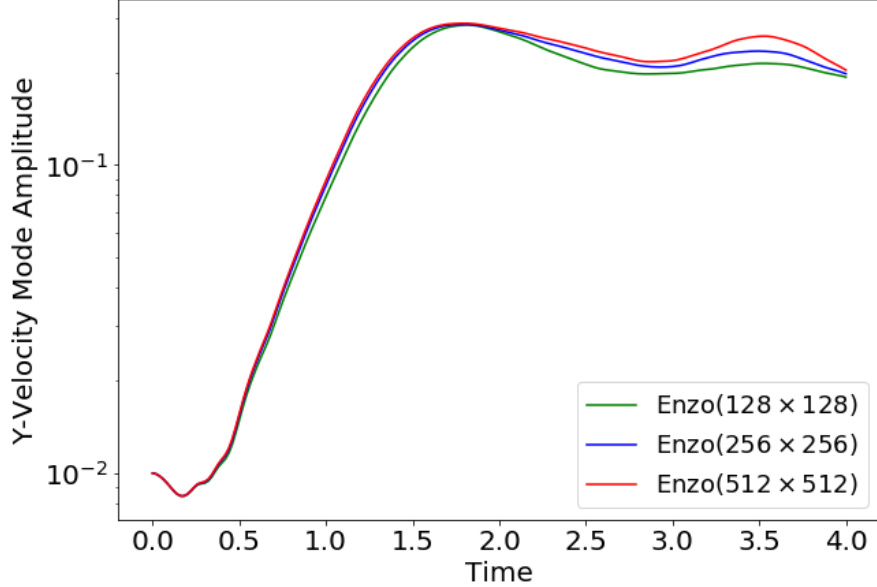
Figure 5: The average y-velocity mode amplitude over all grids versus time for 3 resolutions within time interval $t \in (0, 4)$.

Figure 5 plots the same variables as Figure 4, but for longer time period. The analytical and reference solutions are not applied in non-linear regime, thus not included in this figure.

After about $t = 1.5$, y-velocity amplitude results for all 3 resolutions show a slow oscillating behavior. Figure 2 shows instabilities that are also generated in this non-linear regime. Recently people also look into the performance of numerical simulations in this non-linear regime, since a secondary instability could arise and interests have been developed into exploring the physical explanations thereof.

4 Discussion

4.1 Distinction between Enzo and Analytical Solutions

In this section, we would discuss the possible explanations for the difference between Enzo and analytical results.

4.1.1 Smooth transitions in Density and Velocity across the Interface

As mentioned previously, the analytical solution is calculated for a sharp transition on the Interface (discontinuity). However, Enzo simulation imposes smooth transitions (gradient) in density and velocity across the interface.

Wang, Ye, and Li [18] discusses the influence of gradient in density and velocity on the y-velocity growth rate.

First, we only apply density gradient, keep velocity to be a sharp transition on the interface, and use L_ρ, L_u to define smooth parameters in density and velocity respectively. So in this case $L_\rho \neq 0$, $L_u = 0$. The new analytical growth rate is defined as [18]:

$$r = \left(\frac{\rho_1 \rho_2 \Delta\omega^2}{(\rho_1 + \rho_2)^2} - \frac{A\Delta\omega(\bar{\omega} - \omega_0)}{1 + 1/kL_\rho} - \frac{A^2 \Delta\omega^2}{4(1 + 1/kL_\rho)^2} \right)^{1/2} \tag{37}$$

where $A = (\rho_1 - \rho_2)/(\rho_1 + \rho_2)$ $\Delta\omega = k(V_1 - V_2)$, $\bar{\omega} = k(V_1 + V_2)/2$, and $\omega_0 = k(\rho_1 V_1 + \rho_2 V_2)/(\rho_1 + \rho_2)$.

The first term is the square of the original growth rate without smooth density transition: 35.094. Plugging in the initial conditions in our simulation, the second term under the square root is -2.097, the third term is 0.251. Therefore, for KHI, increasing smooth parameter in density would lead to an increase in y-velocity growth rate (Figure 6).
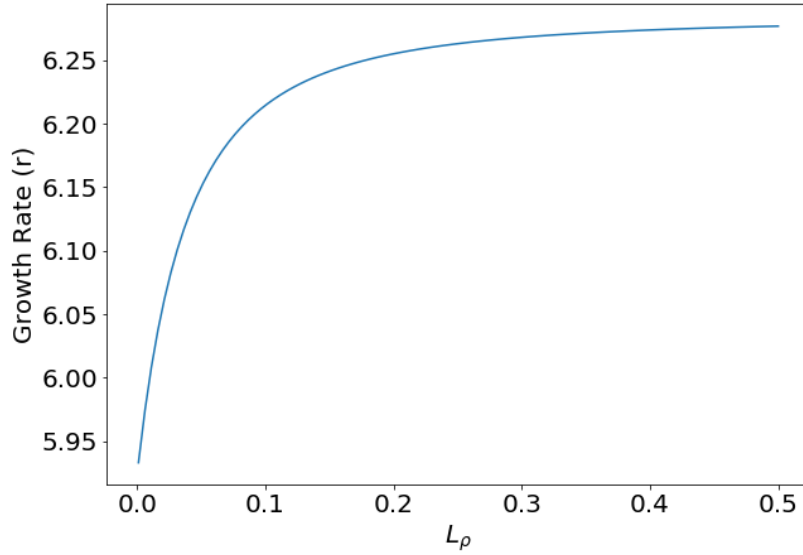

Figure 6: Growth rate (r) versus smooth parameter in density transition layer (L_ρ).

Then, we apply only velocity gradient and keep density to be a sharp transition on the interface. So in this case $L_\rho = 0$, $L_u \neq 0$. The new analytical growth rate is defined as [18]:

$$r = \left(\frac{\rho_1 \rho_2 \Delta\omega^2}{(\rho_1 + \rho_2)^2} - \frac{A^2 \Delta\omega^2}{4(1 + 1/kL_u)^2} - \frac{2}{1 + 1/kL_u} \frac{\rho_1 \rho_2 \Delta\omega^2}{(\rho_1 + \rho_2)^2} + \frac{\Delta\omega^2}{4(1 + 2/kL_u)} \right)^{1/2} \tag{38}$$

where $A = (\rho_1 - \rho_2)/(\rho_1 + \rho_2)$ $\Delta\omega = k(V_1 - V_2)$. The first term is the square of the original growth rate without smooth velocity transition: 35.094. Plugging in the initial conditions in our simulation, the second term under the square root is 0.251, the third term is 16.779, the fourth term is 5.359. Therefore, for KHI, increasing smooth parameter in velocity would lead to a decrease in the y-velocity growth rate (Figure 7).
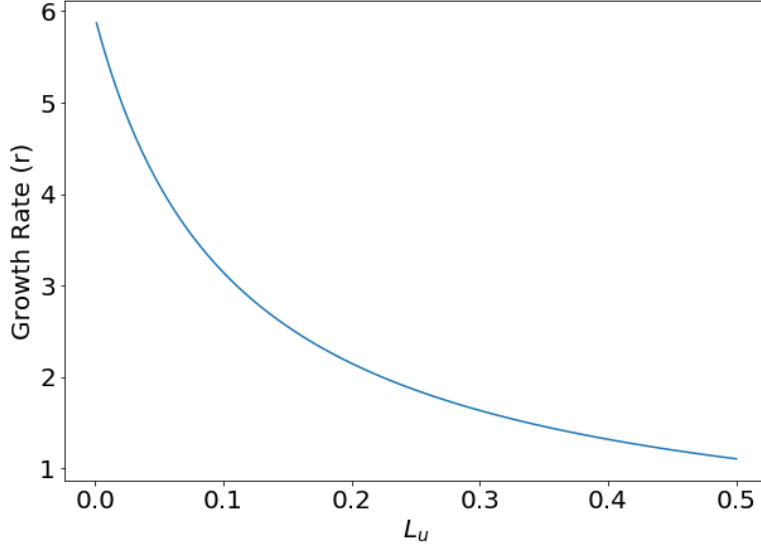
Figure 7: Growth rate (r) versus smooth parameter in velocity transition layer (L_u).

Therefore, gradient in density and velocity have opposite effect on the overall growth rate. We then evaluate the combined effects of velocity and density gradients on the overall growth rate [18]:

$$
\begin{aligned}
r = \Bigg[& \frac{\rho_1 \rho_2 \Delta\omega^2}{(\rho_1 + \rho_2)^2} - \frac{A\Delta\omega(\bar{\omega} - \omega_0)}{1 + 1/kL_\rho} - \frac{A^2\Delta\omega^2}{4(1 + 1/kL_\rho)^2} - \frac{A^2\Delta\omega^2}{4(1 + 1/kL_u)^2} \\
& - \frac{2}{1 + 1/kL_u}\frac{\rho_1\rho_2\Delta\omega^2}{(\rho_1 + \rho_2)^2} + \frac{\Delta\omega^2}{4(1 + 2/kL_u)} + \frac{A\Delta\omega(\bar{\omega} - \omega_0)}{1 + 1/kL_\rho + 1/kL_u} \\
& - \frac{A^2\Delta\omega^2}{4(1 + 1/kL_\rho + 1/kL_u)^2} - \frac{A^2\Delta\omega^2}{2(1 + 1/kL_\rho)(1 + 1/kL_u)} \\
& + \frac{A^2\Delta\omega^2}{2(1 + 1/kL_\rho)(1 + 1/kL_\rho + 1/kL_u)} + \frac{A^2\Delta\omega^2}{2(1 + 1/kL_u)(1 + 1/kL_\rho + 1/kL_u)} \Bigg]^{1/2}
\end{aligned}
\tag{39}
$$

By plugging into the initial conditions used in Enzo simulations, the new growth rate for combined gradients is $r = 5.142$, a 13% reduction comparing to the original classical growth rate (the yellow line on Figure 8).
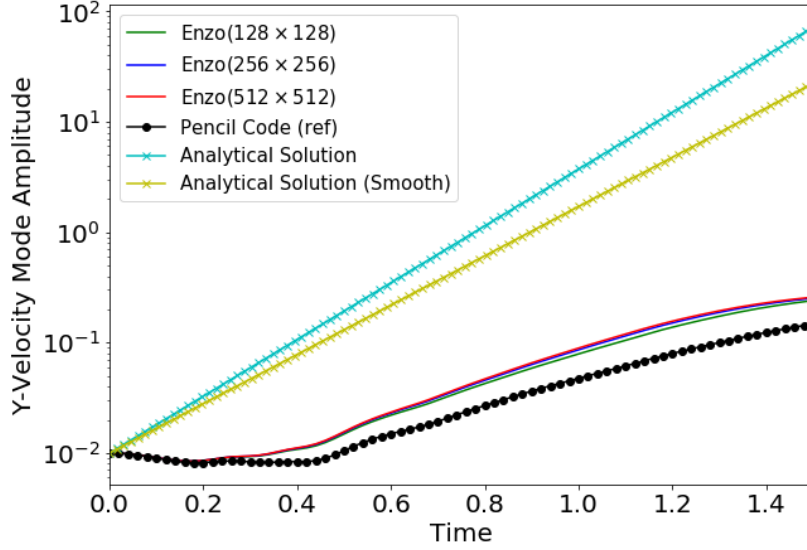
Figure 8: The average y-velocity mode amplitude of all grids versus time. The green, blue and red lines denote Enzo result with different resolutions. The black dotted line shows reference result. The cyan color line represents analytical growth rate solution ($r = 5.924$). The yellow line represents analytical growth rate with smooth transition layers in density and velocity ($r = 5.142$).

4.1.2 Compressible Flow

In analytical solution, we assume that the flow is incompressible. However, in Enzo simulation, the flow is compressible. The influence of compressibility can be qualitatively explained using the Bernoulli's Equation [5].

For incompressible flow, the density is constant, the continuity equation requires that:

$$\rho A V = Constant \tag{40}$$

where A is the cross-section area, V is velocity. Then Bernoulli's equation requires that:

$$\frac{1}{2}V^2 + \Psi + \frac{P}{\rho} = Constant \tag{41}$$

where Ψ represents specific gravitational potential energy. When there's a perturbation on the interface as in Figure 9, on top of the perturbation in region 1, the size of the cross-section decreases, and thus velocity increases due to equation 40. Then according to the Bernoulli's Equation, potential energy does not change substantially, so we could ignore the second term on the left-hand side of equation 41. Then, the increase in velocity would result in a decrease in pressure in region 1 which further enhancing the displacement into region 1 (Figure 9).

15

However, in the compressible flow, the Bernoulli's Equation takes a slightly different form to include compressibility:

$$\frac{1}{2}V^2 + \Psi + \int_{P_1}^{P} \frac{dp}{\rho(p)} = Constant \tag{42}$$

But the general relation between variables stay the same: when perturbation arises, the cross-section area in region 1 decreases, leading to both increases in density and velocity of the flow, thus the velocity increase would be slower comparing to the incompressible flow. Applying Bernoulli's Equation, it is clear that both velocity and density increases, leading to a slower decrease of pressure in region 1. Thus, the overall effect would be a smaller growth rate in Enzo simulation.
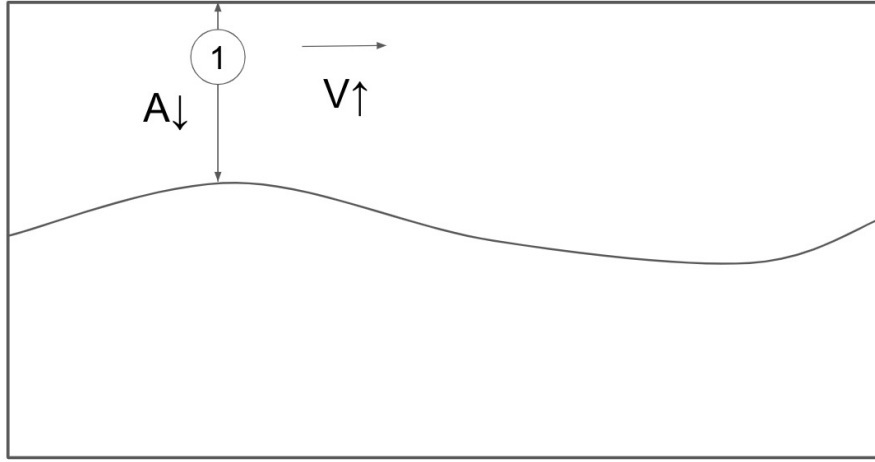

Figure 9: Schematic plot for showing the effect of displacement in the y-direction and Bernoulli's Effect.

4.1.3   Effect of Spatial Resolution

We discussed two physical reasons that can account for the difference between analytical and Enzo solutions above. There are also numerical reasons for the difference and the effect of spatial resolution is one of them.

Figure 10 plots the same variables within the same time periods as Figure 4, but we only focus on the Enzo result here. The Enzo results for 3 different resolutions are close to one another. However, we can still identify that with higher resolution, the y-velocity mode amplitude would be slightly higher, thus a little bit closer to the analytical solution. The small difference between Enzo results show that comparing to the physical reasons discussed above, this numerical effect is not the dominant factor.
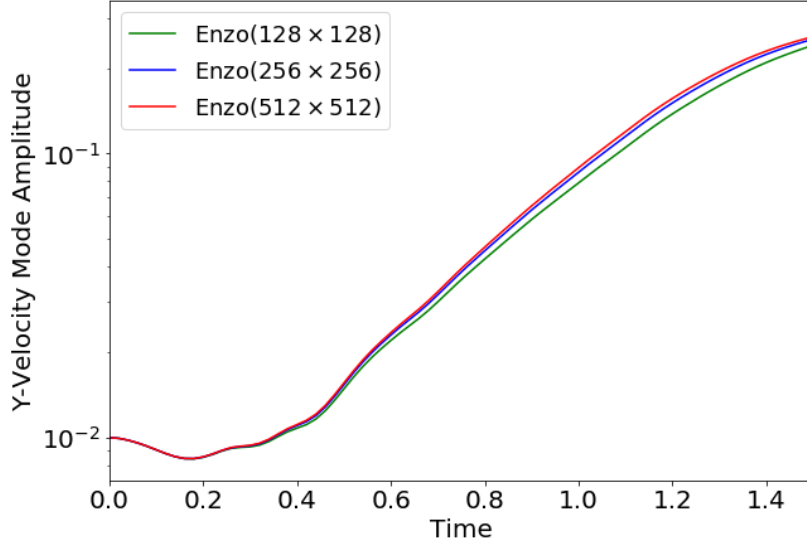
Figure 10: The average y-velocity mode amplitude over all grids versus time. The green, blue and red lines denote Enzo result with different resolutions.

4.1.4 Further Evaluation of Enzo Performance

We would like to conclude on the growth rate we calculated from different parts in this report.

For incompressible flow with sharp transitions, the growth rate is $r_a = 5.924$. For incompressible flow with smooth transitions, the calculated analytical growth rate is $r_s = 5.142$. For Enzo simulation of all resolutions, the growth rate roughly converge to $r_e = 3.140$. Therefore, the growth rate of analytical solution for incompressible flow is roughly 1.89 times that of Enzo result. Besides, considering smooth transition would reduce the growth rate of analytical solution by 13%.

Tricco [15] stated that according to their initial condition (different from ours) and numerical solution, their the analytical growth rate for incompressible flow is roughly 2 times that of the numerical result.

Therefore, our Enzo numerical result is within a reasonable range.

4.2 Distinction between Enzo and Reference Solutions

We evaluate the difference between Enzo and Reference Pencil Code solutions by fitting a curve to the y-velocity mode amplitude value over time for evaluating the exponential growth rate. Since at the beginning of evolution, the growth is slow, and maybe more sensitive to noise, and at the end, the curves become smoother and gradually enter the non-linear growth rate regime, we choose the time interval from $t = 0.3$ to $t = 1.3$ for curve fitting. The growth

rate for Pencil Code reference result is 2.632, the growth rate for Enzo result is 3.140, deviating from the reference result by around 20%.

Since we impose the same initial conditions on the grids for both Enzo and reference solutions. The difference between them could be explained by the difference in the order of accuracy in finite-difference scheme, the use of different solvers, and some other inherent differences in code structures.

4.3 Secondary Instability

In figure 2, we demonstrate that there are secondary instabilities displayed inside the primary KHI billows. The 128×128 grid points simulation does not show this secondary instability due to its low resolution. But, in both 256×256 and 512×512 grids, this instability exists. Therefore, the discussion in this subsection would focus on grids of 256×256 and 512×512.

There has been discussions about whether the secondary instability is a physical reality or an artifact from numerical simulation. Even though the secondary instability is likely to exist in reality, it is hard to be identified in our numerical simulation due to the influence of numerical artifacts. For the instability to be identified as a real-world effect, we would hope to see this instability at the same time, position, with a particular mode in simulations of both 128×128 and 256×256 resolutions [10].

Numerical simulations could lead to the artifact that resembles the formation of secondary instabilities, because as the primary instability develops with time, the interface layer would become thinner. If the size of the interface layer approaches the grid size in simulation, there would be instabilities developed numerically due to the loss of the ability to resolve interfaces [10].

As for our simulation, comparing the secondary instabilities in grids of 256×256 and 512×512, we found out that the secondary instability in the 256×256 grids arise around $t = 2.5$ (Figure 11). However, the secondary instability in the 512×512 grids arise around $t = 2.3$, and the wave lengths of the instability in the 512×512 grids is longer than that in the 256×256 grids. Therefore, the secondary instabilities in these two resolutions arise at different times with different wave lengths (Figure 11-12).
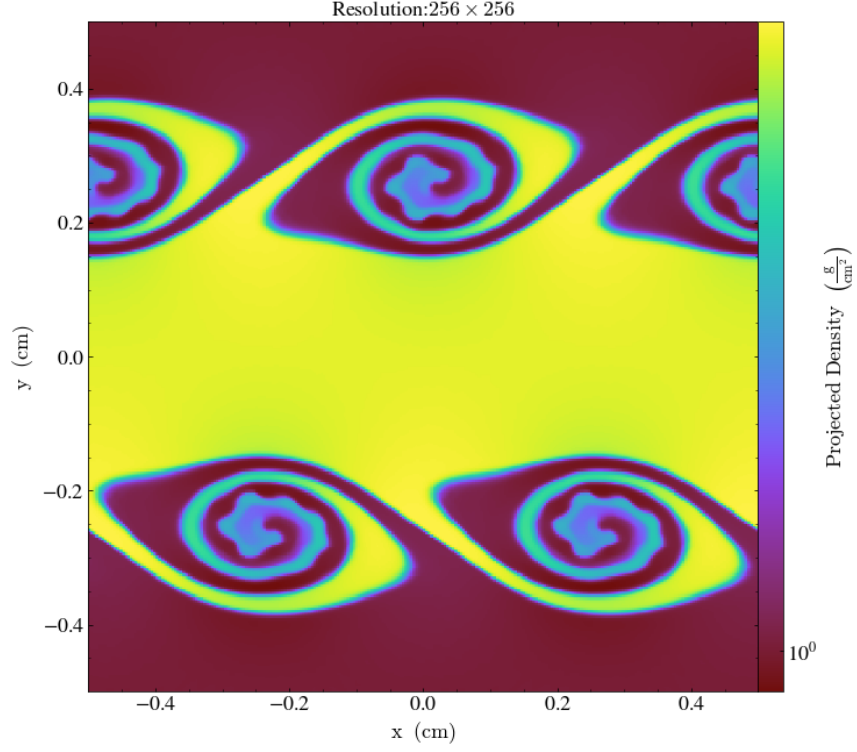
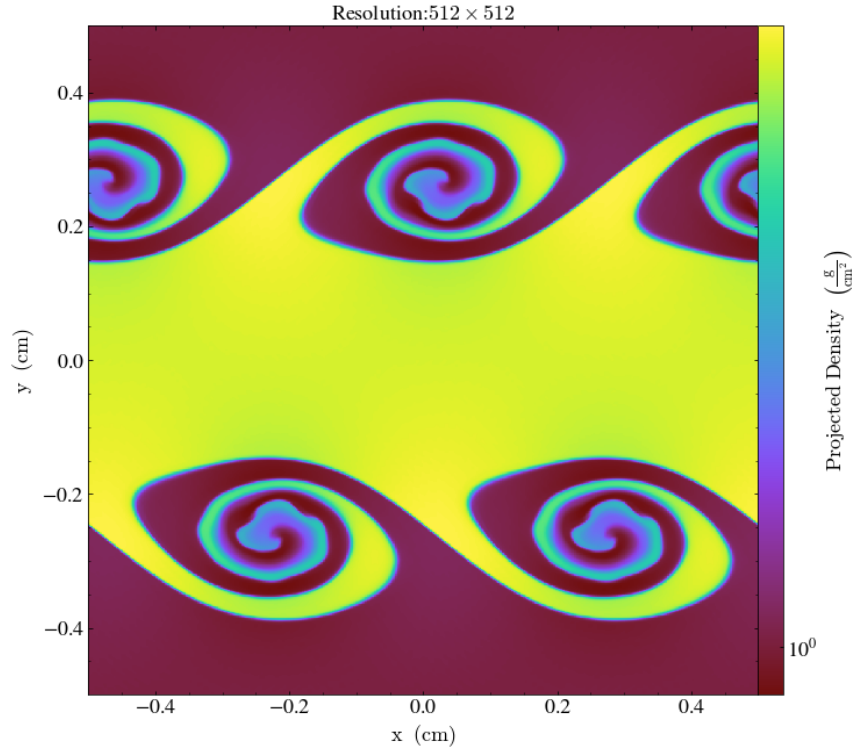Figure 11: Density plot over all grids for resolution of 256×256 when $t = 2.5$.

Figure 12: Density plot over all grids for resolution of 512×512 when $t = 2.3$.

Therefore, the secondary instabilities displayed in our simulation result come from the numerical artifacts and could not be used to determine the existence of secondary instability in reality.

5 Conclusion

We compare Enzo simulation results of KHI with analytical solution and a numerical reference solution run in Pencil Code. The metrics we used to compare results are maximum y-direction specific kinetic energy and y-velocity mode amplitude. The differences between Enzo and analytical results can be explained by both physical and numerical reasons. The difference between Enzo and reference solution can be partially explained by the use of different solvers, order of accuracy of the finite-difference scheme and inherent code structures.

Our work is constrained by the limit of computing power. More complete comparison and thorough analysis could be achieved by increasing resolutions and trying other hydro-methods in Enzo. We haven't applied the Adaptive Mesh Refinement (AMR) method in Enzo for KHI simulation, since the inclusion of AMR would lead to some difficulties for calculating the y-velocity mode amplitude. In equations 6-9, the y-velocity mode amplitude is calculated for distinct grid positions, therefore, applying AMR would smooth the grid boundaries and require modifications to this post-simulation analysis metric. However, in the future evaluations that include AMR would be helpful for better understanding Enzo performance for KHI and related hydrodynamic problems.

Besides, other open source hydrodynamics codes are also recommended to use for testing numerical KHI results, providing some guidance for choosing appropriate methods and codes when conducting more advanced astrophysical research.

Acknowledgement

References

[1] Astropy Collaboration et al. "Astropy: A community Python package for astronomy". In: 558, A33 (Oct. 2013), A33. DOI: 10.1051/0004-6361/201322068. arXiv: 1307.6212 [astro-ph.IM].

[2] M. Brüggen and W. Hillebrandt. "Mixing through shear instabilities". In: *Monthly Notices of the Royal Astronomical Society* 320.1 (Jan. 2001), pp. 73–82. ISSN: 0035-8711. DOI: 10.1046/j.1365-8711.2001.03951.x. eprint: https://academic.oup.com/mnras/article-pdf/320/1/73/3877043/320-1-73.pdf. URL: https://doi.org/10.1046/j.1365-8711.2001.03951.x.

[3]   Greg L. Bryan et al. "ENZO: AN ADAPTIVE MESH REFINEMENT CODE FOR ASTROPHYSICS". In: *The Astrophysical Journal Supplement Series* 211.2 (2014), p. 19. DOI: 10.1088/0067-0049/211/2/19. URL: https://app.dimensions.ai/details/publication/pub.1026720181%20and%20https://iopscience.iop.org/article/10.1088/0067-0049/211/2/19/pdf.

[4]   Subrahmanyan Chandrasekhar. *Hydrodynamic and hydromagnetic stability.* 1961.

[5]   François Charru. *Hydrodynamic Instabilities.* Ed. by PatriciaTranslator de Forcrand-Millard. Cambridge Texts in Applied Mathematics. Cambridge University Press, 2011. DOI: 10.1017/CBO9780511975172.

[6]   J. D. Hunter. "Matplotlib: A 2D graphics environment". In: *Computing in Science & Engineering* 9.3 (2007), pp. 90–95. DOI: 10.1109/MCSE.2007.55.

[7]   Anders Johansen, Thomas Henning, and Hubert Klahr. "Dust Sedimentation and Self-sustained Kelvin-Helmholtz Turbulence in Protoplanetary Disk Midplanes". In: *The Astrophysical Journal* 643.2 (June 2006), pp. 1219–1232. ISSN: 1538-4357. DOI: 10.1086/502968. URL: http://dx.doi.org/10.1086/502968.

[8]   Thomas Kluyver et al. "Jupyter Notebooks – a publishing format for reproducible computational workflows". In: *Positioning and Power in Academic Publishing: Players, Agents and Agendas.* Ed. by F. Loizides and B. Schmidt. IOS Press. 2016, pp. 87–90.

[9]   Lev Davidovich Landau and E. M. Lifshitz. *Fluid mechanics.* 1959.

[10]   Colin P. McNally, Wladimir Lyra, and Jean-Claude Passy. "A WELL-POSED KELVIN-HELMHOLTZ INSTABILITY TEST AND COMPARISON". In: *The Astrophysical Journal Supplement Series* 201.2 (June 2012), p. 18. ISSN: 1538-4365. DOI: 10.1088/0067-0049/201/2/18. URL: http://dx.doi.org/10.1088/0067-0049/201/2/18.

[11]   P. E. J. Nulsen. "Transport processes and the stripping of cluster galaxies." In: 198 (Mar. 1982), pp. 1007–1016. DOI: 10.1093/mnras/198.4.1007.

[12]   Travis E Oliphant. *A guide to NumPy.* Vol. 1. Trelgol Publishing USA, 2006.

[13]   Brant E. Robertson et al. "Computational Eulerian hydrodynamics and Galilean invariance". In: *Monthly Notices of the Royal Astronomical Society* 401.4 (Jan. 2010), pp. 2463–2476. ISSN: 0035-8711. DOI: 10.1111/j.1365-2966.2009.15823.x. eprint: https://academic.oup.com/mnras/article-pdf/401/4/2463/3915161/mnras0401-2463.pdf. URL: https://doi.org/10.1111/j.1365-2966.2009.15823.x.

[14]   F.H. Shu. *The Physics of Astrophysics: Gas dynamics.* Series of books in astronomy. University Science Books, 1991. ISBN: 9780935702651. URL: https://books.google.com/books?id=50VYSc56URUC.

[15]   Terrence S Tricco. "The Kelvin–Helmholtz instability and smoothed particle hydrodynamics". In: *Monthly Notices of the Royal Astronomical Society* 488.4 (July 2019), pp. 5210–5224. ISSN: 1365-2966. DOI: 10.1093/mnras/stz2042. URL: http://dx.doi.org/10.1093/mnras/stz2042.

[16] M. J. Turk et al. "yt: A Multi-code Analysis Toolkit for Astrophysical Simulation Data". In: *The Astrophysical Journal Supplement Series* 192, 9 (Jan. 2011), p. 9. DOI: 10.1088/0067-0049/192/1/9. arXiv: 1011.3514 [astro-ph.IM].

[17] Pauli Virtanen et al. "SciPy 1.0: Fundamental Algorithms for Scientific Computing in Python". In: *Nature Methods* 17 (2020), pp. 261–272. DOI: https://doi.org/10.1038/s41592-019-0686-2.

[18] L. Wang, Wenhua Ye, and Y. Li. "Combined effect of the density and velocity gradients in the combination of Kelvin–Helmholtz and Rayleigh–Taylor instabilities". In: *Physics of Plasmas* 17 (Apr. 2010). DOI: 10.1063/1.3372843.